Wafer-Scale Oxygen-Doped MoS$_2$ Monolayer

Zheng Wei, Jian Tang, Xuanyi Li, Zhen Chi, Yu Wang, Qinqin Wang, Bo Han, Na Li, Biying Huang, Jiawei Li, Hua Yu, Jiahao Yuan, Hailong Chen, Jiatao Sun, Lan Chen, Kehui Wu, Peng Gao, Congli He, Wei Yang, Dongxia Shi, Rong Yang,* and Guangyu Zhang*

Monolayer MoS$_2$ is an emergent 2D semiconductor for next-generation miniaturized and flexible electronics. Although the high-quality monolayer MoS$_2$ is already available at wafer scale, doping of it uniformly remains an unsolved problem. Such doping is of great importance in view of not only tailoring its properties but also facilitating many potential large-scale applications. In this work, the uniform oxygen doping of 2 in wafer-scale monolayer MoS$_2$ (MoS$_{2-x}$O$_x$) with tunable doping levels is realized through an in situ chemical vapor deposition process. Interestingly, ultrafast infrared spectroscopy measurements and first-principles calculations reveal a reduction of bandgaps of monolayer MoS$_{2-x}$O$_x$ with increased oxygen-doping levels. Field-effect transistors and logic devices are also fabricated based on these wafer-scale MoS$_{2-x}$O$_x$ monolayers, and excellent electronic performances are achieved, exhibiting promise of such doped MoS$_2$ monolayers.

1. Introduction

2D transition metal dichalcogenides (TMDCs) have attracted enormous interests recently due to their excellent electrical/optical properties and versatile applications for wearable devices, photodetectors, sensors, and integrated circuits.[1–6] Doping is an effective strategy to tailor their properties for practical applications. For example, photoluminescence (PL) quenching and bandgap decrease were observed in doped TMDC films;[7–14] doping could also increase their electrical conductivities and catalytic activities.[15–22] Different from the standard approach to dope silicon by ion implantation or diffusion, doping of such thin 2D materials may have many different choices such as element substitution, charge transfer, intercalation, and electrostatic field-effect doping.[23] Among these, substitutional doping could produce stable structures with covalent bonds between the hosting atoms and the doping atoms.

Monolayer MoS$_2$ is a typical 2D TMDC with n-type semiconducting characteristics.[24] Previous results have shown that doping in MoS$_2$ monolayers is able to improve their performances in electronics, optoelectronics, and catalysis.[7,12,15,19,21,22,25–28] Among various types of doping, oxygen

Z. Wei, J. Tang, X. Y. Li, Dr. Z. Chi, Y. Wang, Q. Q. Wang, Dr. N. Li, B. Y. Huang, J. W. Li, Dr. H. Yu, J. H. Yuan, Prof. H. L. Chen, Prof. J. T. Sun, Prof. L. Chen, Prof. K. H. Wu, Prof. W. Yang, Prof. D. X. Shi, Prof. R. Yang, Prof. G. Y. Zhang
Beijing National Laboratory for Condensed Matter
Physics and Institute of Physics
Chinese Academy of Sciences
Beijing 100190, China
E-mail: ryang@iphy.ac.cn; gyzhang@iphy.ac.cn

Z. Wei, J. Tang, X. Y. Li, Y. Wang, Q. Q. Wang, Dr. N. Li, B. Y. Huang, J. W. Li, Dr. H. Yu, J. H. Yuan, Prof. H. L. Chen, Prof. L. Chen, Prof. K. H. Wu, Prof. W. Yang, Prof. D. X. Shi, Prof. R. Yang, Prof. G. Y. Zhang
School of Physical Sciences
University of Chinese Academy of Sciences
Beijing 100190, China

B. Han, Prof. P. Gao
Electron Microscopy Laboratory and International
Center for Quantum Materials
School of Physics
Peking University
Beijing 100871, China

Prof. J. T. Sun
School of Information and Electronics
MIIT Key Laboratory for Low-Dimensional
Quantum Structure and Devices
Beijing Institute of Technology
Beijing 100081, China

Prof. P. Gao
Interdisciplinary Institute of Light-Element Quantum Materials
and Research Center for Light-Element Advanced Materials
Peking University
Beijing 100871, China

Prof. P. Gao
Collaborative Innovation Centre of Quantum Matter
Peking University
Beijing 100871, China

Dr. C. L. He
Institute of Advanced Materials
Beijing Normal University
Beijing 100875, China

Prof. D. X. Shi, Prof. G. Y. Zhang
Beijing Key Laboratory for Nanomaterials and Nanodevices
Beijing 100190, China

Prof. R. Yang, Prof. G. Y. Zhang
Songshan Lake Materials Laboratory
Dongguan, Guangdong 523808, China

substitutional doping has gained a lot of interests recently.[14,17,20] Such doping can be facilitated from the oxygen plasma treatment, UV–ozone exposure, calcination, or spontaneous oxidation in atmosphere, and in situ growth.[14,17,18,29,30] However, oxygen doping has only been investigated in limited sized samples, substitutional oxygen doping of monolayer MoS_2 films at a large scale, e.g., wafer scale, has not been realized yet.

In this work, we show an in situ substitutional oxygen doping of 2 in. wafer-scale MoS_2 monolayers with tunable doping levels. Both ultrafast spectroscopy measurements and first-principles calculations demonstrate that the bandgap decreases with the increased oxygen-doping levels accompanied by a direct-to-indirect band transition. The homogeneity of the oxygen-doped MoS_2 wafers has been studied by atomic force microscope (AFM) images and Raman spectroscopy mapping. Furthermore, field-effect transistors (FETs) and logic devices made from $MoS_{2-x}O_x$ films show improved electronic performances.

2. Results and Discussions

Wafer-scale monolayer $MoS_{2-x}O_x$ films were grown on sapphire substrates by chemical vapor deposition (CVD) using S/MoO_3 as precursors and O_2 as the doping agent. Please see Figure S1a (Supporting Information) for the schematic diagram of the experimental setup. In our previous growth of individual $MoS_{2-x}O_x$ grains,[30] we found that oxygen doping prefers a relative low

deposition temperature, e.g., ≈800 °C, compared with the growth of intrinsic (undoped) MoS_2 films at ≈900 °C. In this study, we optimized the growth parameter to realize the deposition of continuous monolayer $MoS_{2-x}O_x$ films. In particular, we increased the amount of reaction precursors and shortened the distances between reaction precursors and target substrates for increased source concentration and nucleation density. In addition, the MoO_3/S ratio was also increased slightly because MoO_3 is the limiting factor of coverage under this S-abundant atmosphere in the growth chamber. The growth process of wafer-scale monolayer $MoS_{2-x}O_x$ films is illustrated in **Figure 1**a–d. In the initial stage of the growth process, triangular nuclei randomly formed on the surface of sapphire substrates and finally merged to a continuous monolayer film by an enlarging process. Note that, even if we prolonged the growth time, this in situ doping growth process also obeys a typical 2D self-limited growth mode. Unless the first monolayer film is fully covered, no bilayer nuclei would form. This process can be seen in the inset of Figure 1d, which shows the coverage of the monolayer films as a function of growth time up to 50 min.

The AFM image of an as-grown $MoS_{2-x}O_x$ film is shown in Figure 1e with a clean and flat surface. Note that these periodic steps are from the preannealed sapphire substrates. Please also see the photo and AFM images in Figure S1b,c (Supporting Information) for more information. The atomic structure of monolayer $MoS_{2-x}O_x$ film is characterized by both scanning transmission electron microscope (STEM) and scanning tunneling microscope
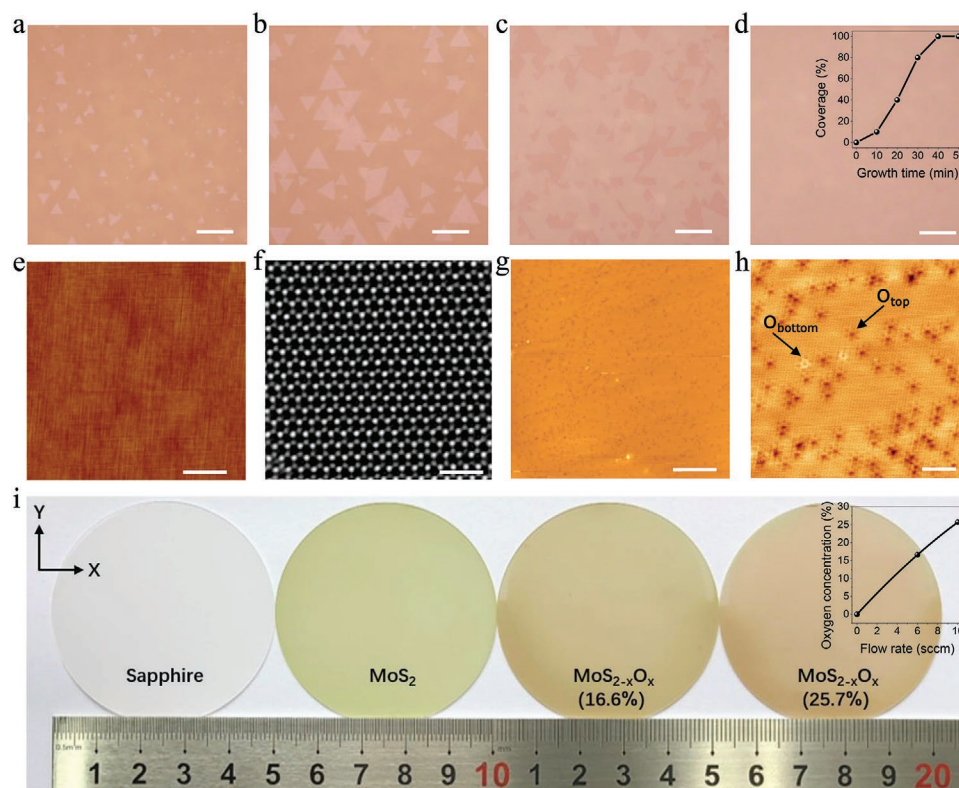
Figure 1. Growth process and characterization of monolayer $MoS_{2-x}O_x$ films. a–d) Optical microscopy images of the growth process. Scale bars: 200 µm. Inset of panel (d) is the coverage of the monolayer films as a function of growth time. e) AFM image of monolayer film. Scale bar: 2 µm. f) STEM image of monolayer film. Scale bar: 1 nm. g,h) STM images of monolayer $MoS_{2-x}O_x$ films. Set points: 2.7 V, 50 pA for panel (g) and 0.75 V, 100 pA for panel (h). Scale bars: 20 and 3 nm, respectively. O_{top} and O_{bottom} are figured out by arrows in panel (h). i) Photos of 2 in wafer-scale sapphire substrate, MoS_2 monolayer, and $MoS_{2-x}O_x$ monolayers with different oxygen concentrations. Inset of panel (i) is the oxygen concentration of the films as a function of oxygen flow rate.

**ADVANCED
SCIENCE NEWS**

www.advancedsciencenews.com

**small
methods**

www.small-methods.com

(STM), and the images are shown in Figure 1f–h. From the STEM image, we can see a nearly perfect lattice structure, and it is difficult to see the oxygen substitution atoms since their atomic number are close to that of sulfur atoms. In contrast, STM images provide clear identification of the oxygen atoms in the top or bottom sulfur atomic layer (also refer to the previous work[31,32]). We can see that most of the substitutional oxygen atoms are on the top layer. Furthermore, the STM images also demonstrated the spatial uniformity of the oxygen dopants from micro perspectives of nanometer magnitude. Please also see the AFM image and high-resolution STM image for $MoS_{2-x}O_x$ monolayers in Figure S2 (Supporting Information).

The oxygen-doping levels are tunable by varying the oxygen flow rates during the growth. Larger oxygen flux would lead to higher concentration of dopants. Figure 1i shows the photos of 2 in. lightly and heavily doped $MoS_{2-x}O_x$ wafers, as well as bare sapphire and intrinsic MoS_2 wafers for comparison. The color of the monolayer films changes from olivine (lightly doped) to umber (heavily doped). The oxygen concentrations of the films estimated by X-ray photoelectron spectroscopy (XPS) are 16.6% and 25.7% for the above shown lightly and heavily doped films, respectively. Please see Figure S3 (Supporting Information) for more information on the XPS spectra and according analysis. The tunability of the doping level is correlated to the oxygen flow rate quantitatively. For example, 6 and 10 sccm high-purity O_2 flowed into the chamber for the growth of $MoS_{2-x}O_x$ films lead to oxygen concentrations of 16.6% and 25.7%, respectively. Inset of Figure 1i shows the oxygen concentration of the films as a function of oxygen flow rate, and the curve is obtained by

the polynomial fitting of the data points. Furthermore, $MoS_{2-x}O_x$ monolayers are also able to grow on double-side-polished sapphire substrates as shown in Figure S4 (Supporting Information).

To investigate the optical spectroscopy properties of the as-grown $MoS_{2-x}O_x$ monolayers, we thus performed Raman and PL spectroscopic investigations. As illustrated in **Figure 2**a, Raman spectra exhibit two typical peaks at $\approx$385.3 cm^{-1} (E_{2g}) and 405.8 cm^{-1} (A_{1g}) in the control sample of the intrinsic monolayer MoS_2 film. In contrast, E_{2g}/A_{1g} peaks of doped films show red/blue shifts. It was also noted that several new Raman peaks located at around 295 and 335 cm^{-1} appear in the doped samples, resulting from the vibrational modes of Mo−O bonds, and the intensity of these peaks increases with the doping levels. In Figure 2b, sharp and strong PL peaks were seen in the intrinsic films, but they quench severely in the oxygen-doped films,[14] especially for the heavily doped one. Note that peaks at $\approx$690 nm are from the sapphire substrates. Compared with the PL peak position of intrinsic MoS_2, the peak position of doped film also shifts to a larger wavelength which suggests the reduced bandgap due to doping.

From macro perspectives, the Raman and PL mapping images (or collective Raman and PL spectra) are effective approaches to show the homogeneity of doped films at large scale. Raman mapping on the doped wafer-scale monolayer $MoS_{2-x}O_x$ film, along the *X*- and *Y*-directions, is shown in Figure 2c,d. Apart from the E_{2g} and A_{1g} peaks, the peaks resulted from oxygen doping are clearly seen and show uniform intensity. Furthermore, Figure 2e,f shows the Raman mapping of the peak located at 295 cm^{-1} and PL mapping of the
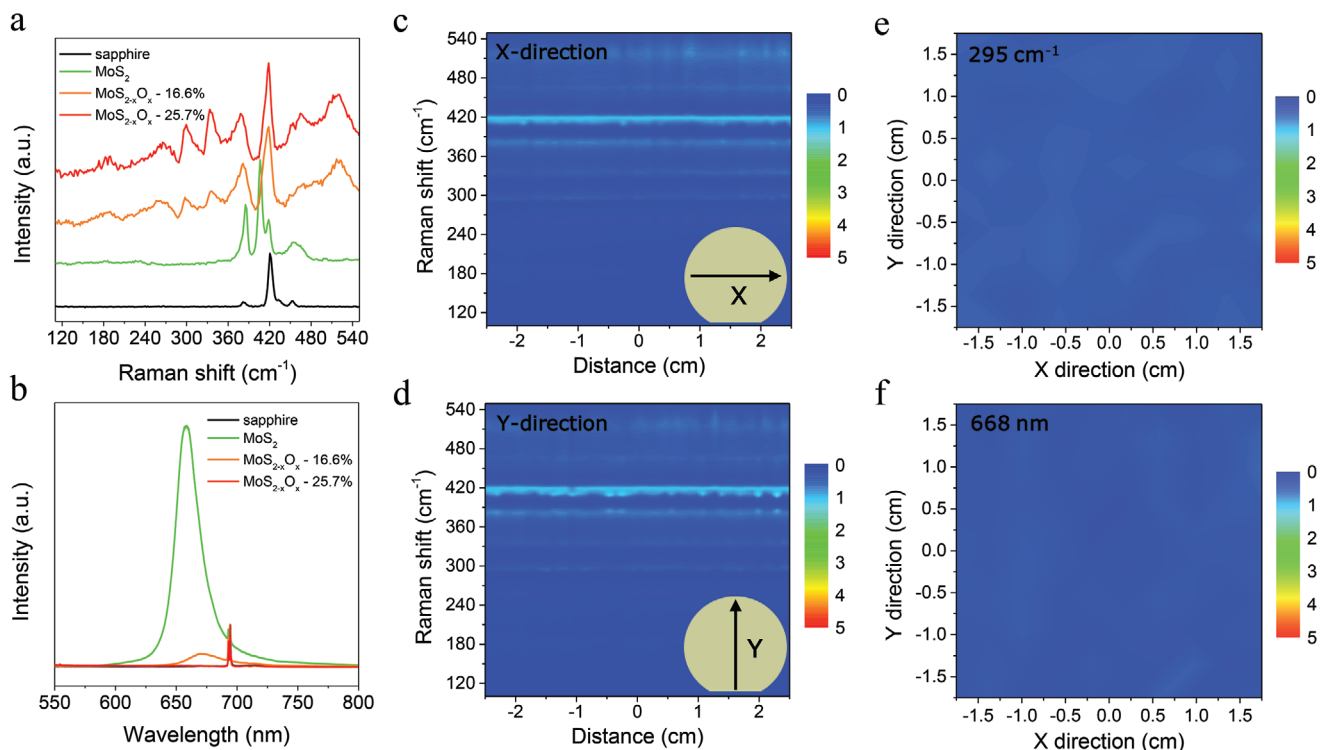
Figure 2. $MoS_{2-x}O_x$ films with tunable oxygen concentrations and homogeneity of wafer-scale monolayer films. a,b) Raman spectra and PL spectra of sapphire substrates, MoS_2 films, and $MoS_{2-x}O_x$ films with different oxygen concentrations. c,d) Raman mapping images of the wafer-scale films along the *X*- and *Y*-directions, respectively. Insets show the *X*- and *Y*-directions for the wafer. e,f) Raman mapping image of the peaks at 295 cm^{-1} and PL mapping image of the peaks at 668 nm, respectively.

ADVANCED
SCIENCE NEWS
www.advancedsciencenews.com

small
methods
www.small-methods.com
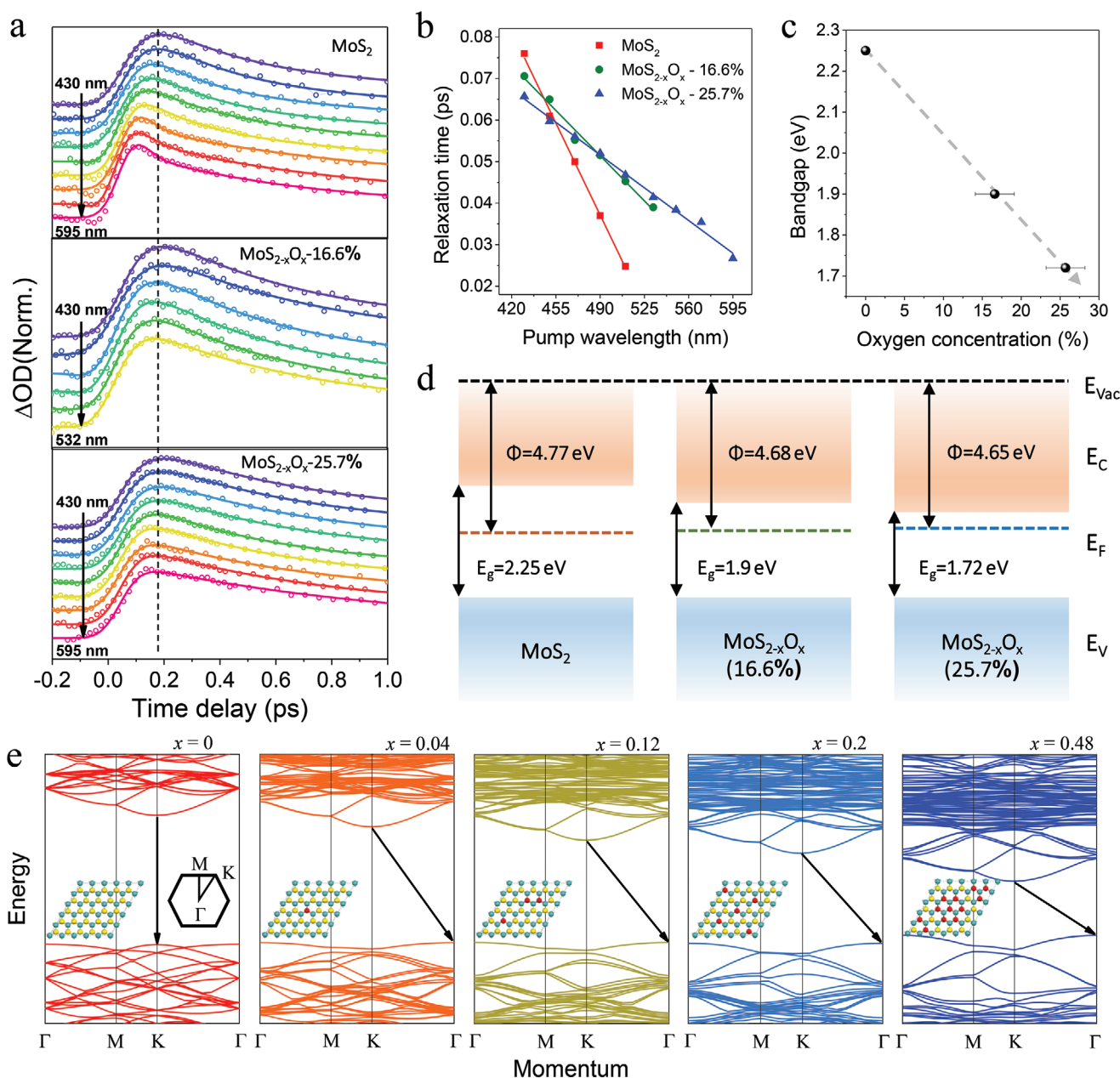
Figure 3. Measurement and calculation of bandgaps and band structures. a) Normalized temporal evolutions' microspectroscopy of MoS_2 and $MoS_{2-x}O_x$ films with different oxygen-doping levels. The dots are the data, and the curves show multiexponential fitting with consideration of the instrument response function (150 fs). b) Hot carrier relaxation times as a function of the pump wavelength that was extracted from panel (a). c) The relationship between bandgaps and oxygen concentration. d) Band diagrams of MoS_2 and $MoS_{2-x}O_x$ films with different oxygen-doping levels. e) Theoretically calculated band structures of $MoS_{2-x}O_x$ with oxygen concentration x varying from 0 to 0.48.

peak at 668 nm across the whole wafer. The nearly consistent contrast in both Raman and PL mapping images illustrates the high homogeneity of oxygen-doped monolayer films. The normalized raw data of the Raman spectra and PL spectra are shown in Figure S5 (Supporting Information).

In order to determine the bandgap of the as-grown $MoS_{2-x}O_x$ films, we thus performed excitation-energy-scanning ultrafast infrared microspectroscopy measurements.[33,34] Similar to the previous method, we used pump pulses to excite electrons at momentum space from the valence band into the conductance band with the phonon energy larger than the

bandgap of $MoS_{2-x}O_x$. **Figure 3**a shows normalized temporal evolutions' microspectroscopy of MoS_2 and $MoS_{2-x}O_x$ films with different oxygen-doping levels. The rapid exponential rises of signals gradually accelerate at relatively longer pump wavelengths for all the measured samples, which reflects the initial intraband relaxation process for the excitation-induced hot carriers. Through monitoring the hot carrier relaxation time exponentially fitted from the rising edges of these spectra, we found that the relaxation time has an inverse linear relationship with the pump wavelength. The intraband hot carrier relaxation time should trend to zero as the pump photon

energy is tuned to realize the band edge excitation. Thus, we can extrapolate the bandgap energy when the relaxation time approaches to zero. Figure 3b shows the corresponding relaxation time fitted at different pump wavelengths. The bandgaps of monolayer $MoS_{2-x}O_x$ can be significantly tuned from 1.9 eV (oxygen concentration: 16.6%) to 1.72 eV (oxygen concentration: 25.7%), compared with the bandgap of intrinsic monolayer MoS_2 (2.25 eV). These results reveal that oxygen doping can effectively reduce the intrinsic bandgap of monolayer MoS_2. Figure 3c clearly shows that the bandgaps decrease monotonically with the increasing oxygen concentrations in the films. In the $MoS_{2-x}O_x$ monolayers, some of the sulfur atoms are substituted by the oxygen atoms. The length of Mo—O bond (2.29 Å) is a little shorter than that of the Mo—S bond (2.41 Å),[30] which leads to in-plane tensile strain and out-plane compressive strain. For MoS_2, both tensile strain and compressive strain reduce the bandgap according to previous results,[35,36] so strain might be the reason for the reduction of bandgaps. Higher doping level of $MoS_{2-x}O_x$ leads to larger strain, and thus smaller bandgap. We also measured the contact potential difference (CPD) by scanning Kelvin probe force microscopy (SKPM) and calculated the work function Φ of different samples by the equation $CPD = (\Phi_{tip} - \Phi_{sample})/e$.[15] Please see Figure S6 (Supporting Information) for the SKPM images. Figure 3d shows the band diagrams of MoS_2 and $MoS_{2-x}O_x$ films with different oxygen-doping levels. The work function also shows a decreasing tendency with the increasing doping levels from 4.77 eV (intrinsic) to 4.68 eV (lightly doped) and 4.65 eV (heavily doped).

We further simulated the band structure of monolayer $MoS_{2-x}O_x$ by first-principles calculations. The calculations were performed on a series of monolayer MoS_2 supercells with some sulfur atoms randomly substituted by oxygen atoms under various doping levels, and the results are shown in Figure 3e. We can see that the conduction band minimum (CBM) remains at the K point for both intrinsic MoS_2 and the doped one, while the valence band maximum (VBM) shifts from the K point to the Γ point for $MoS_{2-x}O_x$ monolayers compared with MoS_2 monolayers, which leads to an transition of direct-to-indirect bandgap. Furthermore, we find that the doping of O atoms with high electronegativity induces charge transfer from Mo atoms to O atoms. The change of charge density distributions of $MoS_{2-x}O_x$ films affects the electronic structure and reduces the bandgap. Therefore, $MoS_{2-x}O_x$ is characterized as a narrowed indirect bandgap semiconductor, and their bandgaps decrease with the increment of oxygen-doping levels. In addition, the formation of indirect bandgap results in the reduction of PL intensity and even quenching as mentioned above. The calculation results are fully consistent with our experimental observations.

Next, we characterized the electrical properties of the synthesized monolayer $MoS_{2-x}O_x$ films. First, we transferred these lightly doped films onto Al_2O_3/Si substrates and fabricated back-gate FETs. **Figure 4**a shows a wafer-scale array of $MoS_{2-x}O_x$ FETs, and inset is the optical microscopy image of a single device. The transfer and output characteristic curves of a typical device at room temperature with a channel length/width of 20/20 µm are shown in Figure 4b,c, respectively. From the transfer curves, we can see that the transistor shows a typical n-type semiconductor behavior with high on/off ratio. Note that
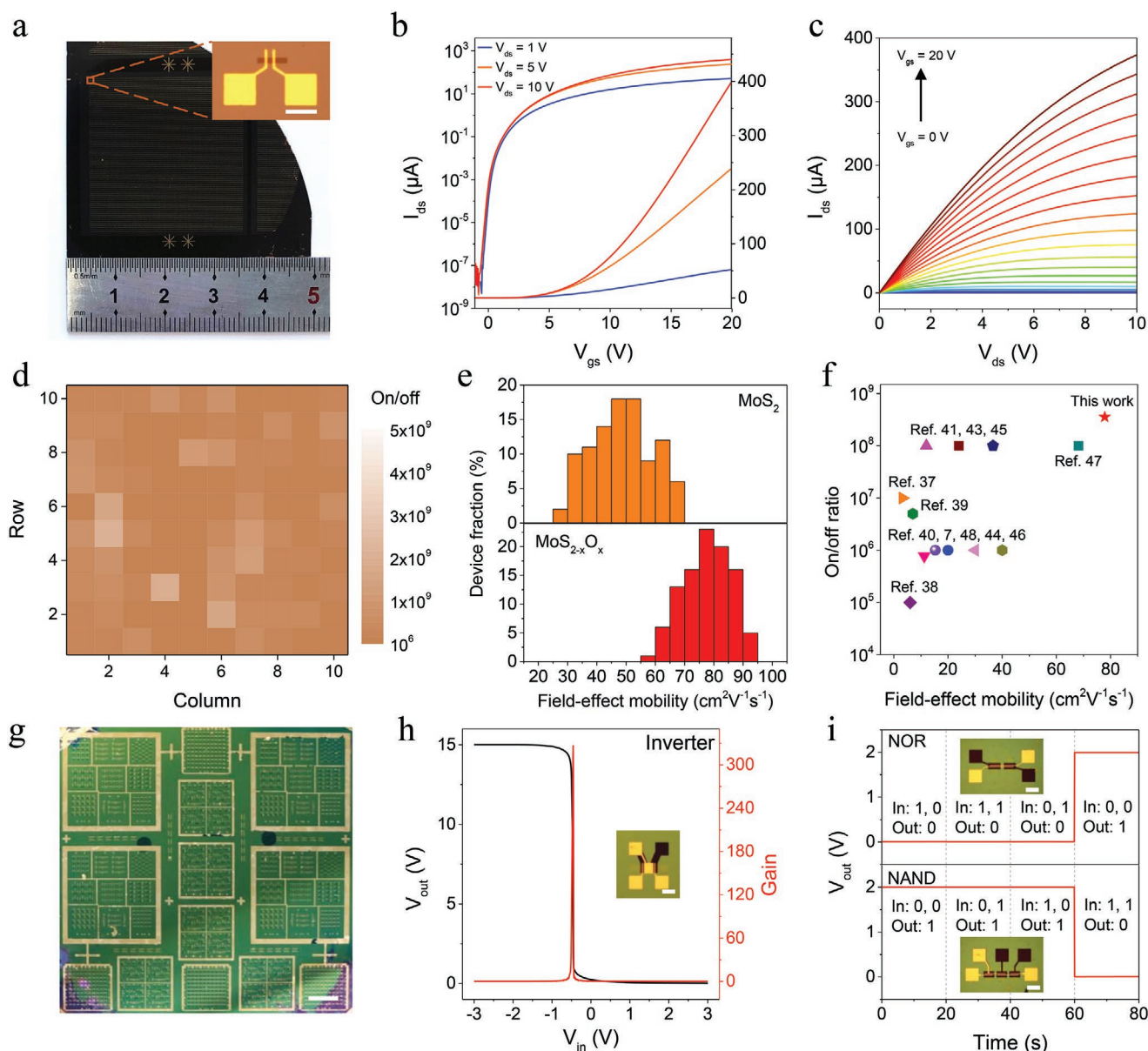
the threshold voltage is negative due to the n-doping of oxygen. As for the output curves, source–drain currents change linearly with the bias voltage, especially at low bias voltages, suggesting Ohmic contacts between the monolayer $MoS_{2-x}O_x$ films and the electrodes.

We further measured 100 devices to figure out the statistic electrical performances. The spatial distribution of current on/off ratio (Figure 4d) shows high homogeneity and averages at 3.5×10^8. We calculated the field-effect mobilities from the equation $\mu = [dI_{ds}/dV_{gs}] \times [L/(WC_iV_{ds})]$, where μ is the field-effect mobility and C_i is the capacitance of the dielectric layer per unit area.[24] Statistics of the distribution of field-effect mobility for the $MoS_{2-x}O_x$ devices are presented in Figure 4e. We also measured intrinsic MoS_2 FETs for comparison. Please also see Figure S7 (Supporting Information) for the detailed transfer characteristic curves and the comparison of specific figures of field-effect mobility between MoS_2 and $MoS_{2-x}O_x$. The variation of mobility is introduced from two main factors. One comes from the inhomogeneity of grain boundaries and vacancy defects. For the channels at different locations with different geometry, the amounts of grain boundaries and defects are not exactly the same, which leads to a variation of mobility, partially. Another factor comes from the device fabrication variations including contact and contamination issues. Contacts are sensitive to interface quality, and residual photoresists at the interfaces are unavoidable during the fabrication process. Through calculating the statistics data, we can obtain that the mobility averages at 78 $cm^2 V^{-1} s^{-1}$ for $MoS_{2-x}O_x$ FETs; while it averages at 48 $cm^2 V^{-1} s^{-1}$ for intrinsic MoS_2 FETs. The increase of electron mobility for $MoS_{2-x}O_x$ monolayers mainly comes from the decrease of bandgap compared with that of intrinsic MoS_2 monolayers. The decrease of bandgap leads to higher conductivity and higher on-state current of the films under the same measurement conditions, which means larger field-effect mobility. Figure 4f shows the comparison of current on/off ratio and mobility between $MoS_{2-x}O_x$ in this work and other films in previous works. From these results, we can see that $MoS_{2-x}O_x$ monolayers show better device performances than other films including intrinsic MoS_2, charge-transfer doped MoS_2, ternary $MoS_{2(1-x)}Se_{2x}$, and $WS_{2x}Se_{2-2x}$.[7,37–48]

Apart from individual FETs, we also used these monolayer $MoS_{2-x}O_x$ films for fabrication of logic devices, including the inverter, NOR gate, and NAND gate. Figure 4g shows such large-scale logic devices with schematics of these electronic circuits shown in Figure S8a–c (Supporting Information). Figure 4h shows the output voltage of the inverter as a function of the input voltage (please also see Figure S8d in the Supporting Information), and the voltage gain shows a high value of 326.5 at $V_{DD} = 15$ V. The output voltages of NOR and NAND gates at four typical input states are shown in Figure 4i. These results also confirm that $MoS_{2-x}O_x$ films are promising candidates for high-performance integrated circuits.

3. Conclusion

In this work, we realized the wafer-scale growth of monolayer $MoS_{2-x}O_x$ films on 2 in. sapphire substrates.

2100091 (5 of 8)

**ADVANCED
SCIENCE NEWS**

www.advancedsciencenews.com

**small
methods**

www.small-methods.com

Figure 4. Back-gate FETs and logic devices of $MoS_{2-x}O_x$ films. a) A wafer-scale array of $MoS_{2-x}O_x$ FETs. Inset: optical microscopy image of single device. Scale bar: 100 μm. b,c) Transfer curves and output curves of $MoS_{2-x}O_x$ FET. d) Spatial distribution of current on/off ratio of the array. e) Statistics of field-effect mobility for MoS_2 and $MoS_{2-x}O_x$. f) Comparisons of field-effect mobility and on/off ratio between this work and previous works. g) Large-scale logic devices. Scale bar: 3 mm. h) Output voltage V_{out} and voltage gain of the $MoS_{2-x}O_x$ logic inverter as a function of the input voltage V_{in}. Inset: optical microscopy image of the logic inverter. Scale bar: 100 μm. i) Output voltage V_{out} of the $MoS_{2-x}O_x$ logic NOR and NAND gates at four typical input states. Inset: optical microscopy images of logic NOR and NAND gates. Scale bars: 100 μm.

Oxygen concentrations in the $MoS_{2-x}O_x$ films are tunable by controlling the oxygen flow rate during the growth process. Both experimental characterizations and theoretical calculations on the $MoS_{2-x}O_x$ monolayers confirm that the bandgaps can decrease from 2.25 eV (intrinsic) to 1.72 eV (heavily doped) accompanied by a direct-to-indirect band transition. The excellent doping homogeneity is revealed from AFM images and spectroscopy mapping images as well. Monolayer $MoS_{2-x}O_x$ FETs show improved performances with a high field-effect mobility of 78 cm^2 V^{-1} s^{-1} and a current on/off ratio of 3.5×10^8. Our results indicate that monolayer $MoS_{2-x}O_x$

films are ideal 2D building blocks for high-performance electronics and optoelectronics.

4. Experimental Section

Growth of MoS_2 and $MoS_{2-x}O_x$ Monolayers: The growth of 2 in. wafer-scale monolayer MoS_2 and $MoS_{2-x}O_x$ films was carried out in a three-temperature-zone CVD system. S (Alfa Aesar, 99.5%, 10 g) and MoO_3 (Alfa Aesar, 99.999%, 50 mg) powders were used as reactive precursors and were loaded in two inner quartz tubes at upstream zones I and II, respectively. 2 in. sapphire substrates (*C*-plane off *M*-axis, thickness:

430 µm) were vertically loaded at downstream zone III (Figure S1a, Supporting Information). Sapphire substrates were preannealed at 1000 °C in order to form the atomically flat steps on the surfaces. During the growth process, temperatures at zones I, II, and III were 130, 530, and 900/800 °C, respectively, for the growth of $MoS_2/MoS_{2-x}O_x$. High-purity Ar (275 sccm) was flown through the quartz tubes as carrying gas. For $MoS_{2-x}O_x$ films with the oxygen concentrations of 16.6% and 25.7%, 6 and 10 sccm high-purity O_2 were injected into the chamber during the growth process, respectively. The pressure of the growth chamber was maintained at about 1 Torr, and the whole growth process was lasted for 50 min.

Characterizations of Samples: AFM imaging was performed by Veeco Multimode III system under the tapping mode. STEM samples were prepared by transferring the $MoS_{2-x}O_x$ films from sapphire substrates to grids. The films were first lifted off by deionized water and then fished up by grids from the surface of water. STEM imaging was performed by an aberration-corrected Nion U-HERMES200 microscope operated at 60 kV. STM samples were prepared by direct growth of $MoS_{2-x}O_x$ films on highly oriented pyrolytic graphite substrates. STM imaging was carried out in a low-temperature STM system (4.5 K, 10^{-10} Torr) with chemical-etched W tip. XPS was carried out by Thermo Fisher Scientific ESCALAB 250X with monochromatic Al Kα source (1468.6 eV). SKPM images were performed by Asylum Research Cypher S system with a platinum-coated AFM tip. Raman and PL spectra were performed by Horiba Jobin Yvon LabRAM HR-Evolution Raman system with a 532 nm laser excitation under a power of 500 µW. Excitation-energy-scanning ultrafast infrared microspectroscopy measurements were carried out by a femtosecond amplifier laser system (Spitfire Ace, Spectra Physics) that generated laser pulses with a repetition rate of 1 kHz, 800 nm central wavelength, and a pulse duration of ≈35 fs. Samples for ultrafast infrared microspectroscopy measurements were grown on transparent double-side-polished sapphire substrates.

Band Structure Calculations: First-principles calculations were performed on the basis of density-functional theory (DFT) as implemented in the Vienna ab initio simulation package (VASP).[49] The ions' cores were described by the projector augmented wave (PAW) method,[50] and the exchange-correlation interactions were described by the Perdew–Bruke–Ernzerhof (PBE)[51] parameterization of the generalized gradient approximation (GGA). The energy cutoff for plane waves was set to be 500 eV. The atomic positions were fully optimized until all the free energies were less than 10^{-4} eV before conducting electronic structures calculations.

Device Fabrications and Measurements: FETs and logic devices were fabricated by the standard microfabrication process. For the back-gate transistors, 30 nm high-k Al_2O_3 film was deposited on the heavily doped silicon substrate by atomic layer deposition (ALD) as the dielectric layer. ALD was performed at 150 °C with alternant trimethylaluminum (TMA) pulse and H_2O pulse by Cambridge Savannah-100 ALD system. Monolayer $MoS_{2-x}O_x$ was then transferred from sapphire substrate onto Al_2O_3/Si and followed by the preparation of channels and metal electrodes. The monolayer films were first patterned into ribbons by UV lithography (Suss MicroTec Gmbh MA6) and reactive ion etching (Oxford Instruments Plasma 80 plus). Au/Ti/Au electrodes were patterned by a second UV lithography process and deposited by electron beam evaporation with a thickness of 1/3/30 nm. For the fabrication of logic devices, the experimental methods were the same as those of back-gate devices while the order of fabrication steps changed according to requirement. Electrical measurements of all devices were carried out in a high-vacuum (1×10^{-6} mbar) four-probe-station system by an Agilent 4156C semiconductor parameter analyzer.

Supporting Information

Supporting Information is available from the Wiley Online Library or from the author.

Conflict of Interest

The authors declare no conflict of interest.

Author Contributions

Z.W. and J.T. contributed equally to this work. G.Y.Z. and R.Y. conceived and supervised the project. Z.W., Q.Q.W., and B.Y.H. prepared the MoS_2 and $MoS_{2-x}O_x$ samples. Z.C. and H.L.C. performed the ultrafast infrared spectroscopy. Z.W. and J.H.Y. carried out SKPM. X.Y.L. and J.T.S. calculated the band structures. Y.W., L.C., and K.H.W. carried out STM. J.T. and B.H. performed STEM under the direction of P.G. Z.W. carried out XPS. Z.W., J.T., and J.W.L. performed the ALD. Z.W. and J.T. fabricated and measured the FETs and logic devices. G.Y.Z., R.Y., Z.W., and J.T. analyzed the results and wrote the manuscript. All authors commented on this paper.

Data Availability Statement

Research data are not shared.

[1] M. Chhowalla, H. S. Shin, G. Eda, L. J. Li, K. P. Loh, H. Zhang, *Nat. Chem.* **2013**, *5*, 263.

[2] Q. H. Wang, K. Kalantar-Zadeh, A. Kis, J. N. Coleman, M. S. Strano, *Nat. Nanotechnol.* **2012**, *7*, 699.

[3] S. L. Li, K. Tsukagoshi, E. Orgiu, P. Samori, *Chem. Soc. Rev.* **2016**, *45*, 118.

[4] W. Choi, N. Choudhary, G. H. Han, J. Park, D. Akinwande, Y. H. Lee, *Mater. Today* **2017**, *20*, 116.

[5] O. Lopez-Sanchez, D. Lembke, M. Kayci, A. Radenovic, A. Kis, *Nat. Nanotechnol.* **2013**, *8*, 497.

[6] N. Li, Q. Wang, C. Shen, Z. Wei, H. Yu, J. Zhao, X. Lu, G. Wang, C. He, L. Xie, J. Zhu, L. Du, R. Yang, D. Shi, G. Zhang, *Nat. Electron.* **2020**, *3*, 711.

[7] Y. Gong, Z. Liu, A. R. Lupini, G. Shi, J. Lin, S. Najmaei, Z. Lin, A. L. Elias, A. Berkdemir, G. You, H. Terrones, M. Terrones, R. Vajtai, S. T. Pantelides, S. J. Pennycook, J. Lou, W. Zhou, P. M. Ajayan, *Nano Lett.* **2014**, *14*, 442.

[8] S. Susarla, A. Kutana, J. A. Hachtel, V. Kochat, A. Apte, R. Vajtai, J. C. Idrobo, B. I. Yakobson, C. S. Tiwary, P. M. Ajayan, *Adv. Mater.* **2017**, *29*, 1702457.

**ADVANCED
SCIENCE NEWS**

www.advancedsciencenews.com

**small
methods**

www.small-methods.com

[9] F. Zhang, Y. F. Lu, D. S. Schulman, T. Y. Zhang, K. Fujisawa, Z. Lin, Y. Lei, A. L. Elias, S. Das, S. B. Sinnott, M. Terrones, *Sci. Adv.* **2019**, *5*, 8.

[10] J. Gao, Y. D. Kim, L. Liang, J. C. Idrobo, P. Chow, J. Tan, B. Li, L. Li, B. G. Sumpter, T. M. Lu, V. Meunier, J. Hone, N. Koratkar, *Adv. Mater.* **2016**, *28*, 9735.

[11] F. Cui, Q. Feng, J. Hong, R. Wang, Y. Bai, X. Li, D. Liu, Y. Zhou, X. Liang, X. He, Z. Zhang, S. Liu, Z. Lei, Z. Liu, T. Zhai, H. Xu, *Adv. Mater.* **2017**, *29*, 1705015.

[12] D. Pierucci, H. Henck, Z. Ben Aziza, C. H. Naylor, A. Balan, J. E. Rault, M. G. Silly, Y. J. Dappe, F. Bertran, P. Le Fevre, F. Sirotti, A. T. Johnson, A. Ouerghi, *ACS Nano* **2017**, *11*, 1755.

[13] S. H. Su, Y. T. Hsu, Y. H. Chang, M. H. Chiu, C. L. Hsu, W. T. Hsu, W. H. Chang, J. H. He, L. J. Li, *Small* **2014**, *10*, 2589.

[14] N. Kang, H. P. Paudel, M. N. Leuenberger, L. Tetard, S. I. Khondaker, *J. Phys. Chem. C* **2014**, *118*, 21258.

[15] Y. Kim, H. Bark, B. Kang, C. Lee, *ACS Appl. Mater. Interfaces* **2019**, *11*, 12613.

[16] B. Liu, Y. Ma, A. Zhang, L. Chen, A. N. Abbas, Y. Liu, C. Shen, H. Wan, C. Zhou, *ACS Nano* **2016**, *10*, 5153.

[17] J. Jadwiszczak, C. O'Callaghan, Y. B. Zhou, D. S. Fox, E. Weitz, D. Keane, C. P. Cullen, I. O'Reilly, C. Downing, A. Shmeliov, P. Maguire, J. J. Gough, C. McGuinness, M. S. Ferreira, A. L. Bradley, J. J. Boland, G. S. Duesberg, V. Nicolosi, H. Z. Zhang, *Sci. Adv.* **2018**, *4*, eaao5031.

[18] J. Peto, T. Ollar, P. Vancso, Z. I. Popov, G. Z. Magda, G. Dobrik, C. Hwang, P. B. Sorokin, L. Tapaszto, *Nat. Chem.* **2018**, *10*, 1246.

[19] S. Z. Yang, Y. Gong, P. Manchanda, Y. Y. Zhang, G. Ye, S. Chen, L. Song, S. T. Pantelides, P. M. Ajayan, M. F. Chisholm, W. Zhou, *Adv. Mater.* **2018**, *30*, 1803477.

[20] J. Xie, J. Zhang, S. Li, F. Grote, X. Zhang, H. Zhang, R. Wang, Y. Lei, B. Pan, Y. Xie, *J. Am. Chem. Soc.* **2013**, *135*, 17881.

[21] H. Gao, J. Suh, M. C. Cao, A. Y. Joe, F. Mujid, K. H. Lee, S. Xie, P. Poddar, J. U. Lee, K. Kang, P. Kim, D. A. Muller, J. Park, *Nano Lett.* **2020**, *20*, 4095.

[22] Z. Cai, T. Shen, Q. Zhu, S. Feng, Q. Yu, J. Liu, L. Tang, Y. Zhao, J. Wang, B. Liu, H. M. Cheng, *Small* **2020**, *16*, 1903181.

[23] P. Luo, F. Zhuge, Q. Zhang, Y. Chen, L. Lv, Y. Huang, H. Li, T. Zhai, *Nanoscale Horiz.* **2019**, *4*, 26.

[24] B. Radisavljevic, A. Radenovic, J. Brivio, V. Giacometti, A. Kis, *Nat. Nanotechnol.* **2011**, *6*, 147.

[25] J. Suh, T. L. Tan, W. Zhao, J. Park, D. Y. Lin, T. E. Park, J. Kim, C. Jin, N. Saigal, S. Ghosh, Z. M. Wong, Y. Chen, F. Wang, W. Walukiewicz, G. Eda, J. Wu, *Nat. Commun.* **2018**, *9*, 199.

[26] K. Zhang, B. M. Bersch, J. Joshi, R. Addou, C. R. Cormier, C. Zhang, K. Xu, N. C. Briggs, K. Wang, S. Subramanian, K. Cho, S. Fullerton-Shirey, R. M. Wallace, P. M. Vora, J. A. Robinson, *Adv. Funct. Mater.* **2018**, *28*, 1706950.

[27] A. Azcatl, X. Qin, A. Prakash, C. Zhang, L. Cheng, Q. Wang, N. Lu, M. J. Kim, J. Kim, K. Cho, R. Addou, C. L. Hinkle, J. Appenzeller, R. M. Wallace, *Nano Lett.* **2016**, *16*, 5437.

[28] Q. Ma, M. Isarraraz, C. S. Wang, E. Preciado, V. Klee, S. Bobek, K. Yamaguchi, E. Li, P. M. Odenthal, A. Nguyen, D. Barroso, D. Z. Sun, G. V. Palacio, M. Gomez, A. Nguyen, D. Le, G. Pawin, J. Mann, T. F. Heinz, T. S. Rahman, L. Bartels, *ACS Nano* **2014**, *8*, 4672.

[29] A. Azcatl, S. Kc, X. Peng, N. Lu, S. McDonnell, X. Qin, F. de Dios, R. Addou, J. Kim, M. J. Kim, K. Cho, R. M. Wallace, *2D Mater.* **2015**, *2*, 014004.

[30] J. Tang, Z. Wei, Q. Wang, Y. Wang, B. Han, X. Li, B. Huang, M. Liao, J. Liu, N. Li, Y. Zhao, C. Shen, Y. Guo, X. Bai, P. Gao, W. Yang, L. Chen, K. Wu, R. Yang, D. Shi, G. Zhang, *Small* **2020**, *16*, 2004276.

[31] S. Barja, S. Refaely-Abramson, B. Schuler, D. Y. Qiu, A. Pulkin, S. Wickenburg, H. Ryu, M. M. Ugeda, C. Kastl, C. Chen, C. Hwang, A. Schwartzberg, S. Aloni, S. K. Mo, D. Frank Ogletree, M. F. Crommie, O. V. Yazyev, S. G. Louie, J. B. Neaton, A. Weber-Bargioni, *Nat. Commun.* **2019**, *10*, 3382.

[32] B. Schuler, J. H. Lee, C. Kastl, K. A. Cochrane, C. T. Chen, S. Refaely-Abramson, S. Yuan, E. van Veen, R. Roldan, N. J. Borys, R. J. Koch, S. Aloni, A. M. Schwartzberg, D. F. Ogletree, J. B. Neaton, A. Weber-Bargioni, *ACS Nano* **2019**, *13*, 10520.

[33] Z. Chi, X. Zhang, X. Wen, J. Han, Z. Wei, L. Du, J. Lai, X. Wang, G. Zhang, Q. Zhao, H. Chen, P. M. Ajayan, Y. X. Weng, *J. Phys. Chem. Lett.* **2021**, *12*, 585.

[34] H. Chen, X. Wen, J. Zhang, T. Wu, Y. Gong, X. Zhang, J. Yuan, C. Yi, J. Lou, P. M. Ajayan, W. Zhuang, G. Zhang, J. Zheng, *Nat. Commun.* **2016**, *7*, 12512.

[35] Z. Liu, M. Amani, S. Najmaei, Q. Xu, X. Zou, W. Zhou, T. Yu, C. Qiu, A. G. Birdwell, F. J. Crowne, R. Vajtai, B. I. Yakobson, Z. Xia, M. Dubey, P. M. Ajayan, J. Lou, *Nat. Commun.* **2014**, *5*, 5246.

[36] M. López-Suárez, I. Neri, R. Rurali, *J. Appl. Phys.* **2016**, *119*, 165105.

[37] L. Liu, H. Qiu, J. Wang, G. Xu, L. Jiao, *Nanoscale* **2016**, *8*, 4486.

[38] K. K. Liu, W. Zhang, Y. H. Lee, Y. C. Lin, M. T. Chang, C. Y. Su, C. S. Chang, H. Li, Y. Shi, H. Zhang, C. S. Lai, L. J. Li, *Nano Lett.* **2012**, *12*, 1538.

[39] J. Zhang, H. Yu, W. Chen, X. Z. Tian, D. H. Liu, M. Cheng, G. B. Xie, W. Yang, R. Yang, X. D. Bai, D. X. Shi, G. Y. Zhang, *ACS Nano* **2014**, *8*, 6024.

[40] P. Yang, S. Zhang, S. Pan, B. Tang, Y. Liang, X. Zhao, Z. Zhang, J. Shi, Y. Huan, Y. Shi, S. J. Pennycook, Z. Ren, G. Zhang, Q. Chen, X. Zou, Z. Liu, Y. Zhang, *ACS Nano* **2020**, *14*, 5036.

[41] M. Ju, X. Liang, J. Liu, L. Zhou, Z. Liu, R. G. Mendes, M. H. Rümmeli, L. Fu, *Chem. Mater.* **2017**, *29*, 6095.

[42] H. Yu, Z. Yang, L. Du, J. Zhang, J. Shi, W. Chen, P. Chen, M. Liao, J. Zhao, J. Meng, G. Wang, J. Zhu, R. Yang, D. Shi, L. Gu, G. Zhang, *Small* **2017**, *13*, 1603005.

[43] Z. Zhang, X. Xu, J. Song, Q. Gao, S. Li, Q. Hu, X. Li, Y. Wu, *Appl. Phys. Lett.* **2018**, *113*, 202103.

[44] K. Kang, S. Xie, L. Huang, Y. Han, P. Y. Huang, K. F. Mak, C. J. Kim, D. Muller, J. Park, *Nature* **2015**, *520*, 656.

[45] C. J. Lockhart de la Rosa, A. Nourbakhsh, M. Heyne, I. Asselberghs, C. Huyghebaert, I. Radu, M. Heyns, S. De Gendt, *Nanoscale* **2017**, *9*, 258.

[46] H. Yu, M. Liao, W. Zhao, G. Liu, X. J. Zhou, Z. Wei, X. Xu, K. Liu, Z. Hu, K. Deng, S. Zhou, J. A. Shi, L. Gu, C. Shen, T. Zhang, L. Du, L. Xie, J. Zhu, W. Chen, R. Yang, D. Shi, G. Zhang, *ACS Nano* **2017**, *11*, 12001.

[47] X. Duan, C. Wang, Z. Fan, G. Hao, L. Kou, U. Halim, H. Li, X. Wu, Y. Wang, J. Jiang, A. Pan, Y. Huang, R. Yu, X. Duan, *Nano Lett.* **2016**, *16*, 264.

[48] D. Kiriya, M. Tosun, P. Zhao, J. S. Kang, A. Javey, *J. Am. Chem. Soc.* **2014**, *136*, 7853.

[49] G. Kresse, J. Furthmuller, *Comput. Mater. Sci.* **1996**, *6*, 15.

[50] M. Gajdoš, K. Hummer, G. Kresse, J. Furthmüller, F. Bechstedt, *Phys. Rev. B* **2006**, *73*, 045112.

[51] J. P. Perdew, K. Burke, M. Ernzerhof, *Phys. Rev. Lett.* **1996**, *77*, 3865.